Enhancing Thermoelectric and Mechanical Properties of p-Type (Bi,Sb)2Te3 through Rickardite Mineral (Cu2.9Te2) Incorporation

Kivanc Saglik, Mujde Yahyaoglu, Christophe Candolfi, Umut Aydemir

▶ **To cite this version:**

Kivanc Saglik, Mujde Yahyaoglu, Christophe Candolfi, Umut Aydemir. Enhancing Thermoelectric and Mechanical Properties of p-Type (Bi,Sb)2Te3 through Rickardite Mineral (Cu2.9Te2) Incorporation. Chemistry of Materials, 2023, 35 (9), pp.3603-3613. 10.1021/acs.chemmater.3c00229 . hal-04093868

HAL Id: hal-04093868
https://hal.science/hal-04093868

Submitted on 10 May 2023

HAL is a multi-disciplinary open access archive for the deposit and dissemination of scientific research documents, whether they are published or not. The documents may come from teaching and research institutions in France or abroad, or from public or private research centers.

L'archive ouverte pluridisciplinaire **HAL**, est destinée au dépôt et à la diffusion de documents scientifiques de niveau recherche, publiés ou non, émanant des établissements d'enseignement et de recherche français ou étrangers, des laboratoires publics ou privés.

Distributed under a Creative Commons Attribution 4.0 International License

CHEMISTRY OF MATERIALS

pubs.acs.org/cm

Article

Enhancing Thermoelectric and Mechanical Properties of *p*-Type (Bi, Sb)$_2$Te$_3$ through Rickardite Mineral (Cu$_{2.9}$Te$_2$) Incorporation

Kivanc Saglik, Mujde Yahyaoglu, Christophe Candolfi, and Umut Aydemir*

Cite This: *Chem. Mater.* 2023, 35, 3603−3613

Read Online

ACCESS | Metrics & More | Article Recommendations | Supporting Information

ABSTRACT: Bi$_2$Te$_3$-based alloys are widely utilized in Peltier coolers owing to their highest thermoelectric performance at near-room-temperatures. However, their peak dimensionless thermoelectric figure of merit, zT, is limited to a narrow temperature window due to minority carrier excitation emerging upon heating at around 400 K. Here, we show how this issue can be overcome by incorporating a synthetic rickardite mineral, Cu$_{3-x}$Te$_2$, in *p*-type (Bi, Sb)$_2$Te$_3$. The significant enhancement of the electronic and thermal properties could be achieved due to small Cu incorporation into the crystal structure of (Bi, Sb)$_2$Te$_3$ and homogeneous precipitation of Cu$_{3-x}$Te$_2$ at the grain boundaries. This leads to a high average zT value (zT_{ave}) of 1.22 between 350 and 500 K for two compositions, Bi$_{0.5}$Sb$_{1.5}$Te$_3$ (BST-5) and Bi$_{0.3}$Sb$_{1.7}$Te$_3$ (BST-3), with peak zT values of 1.32 at 467 K and 1.30 at 400 K, respectively. These high zT values result in a considerably high maximum device ZT of ca. 1.15 and a theoretical efficiency of up to 7% between 325 and 525 K. Additionally, room-temperature micro-hardness is substantially improved, which is desirable for constructing reliable and durable thermoelectric modules.

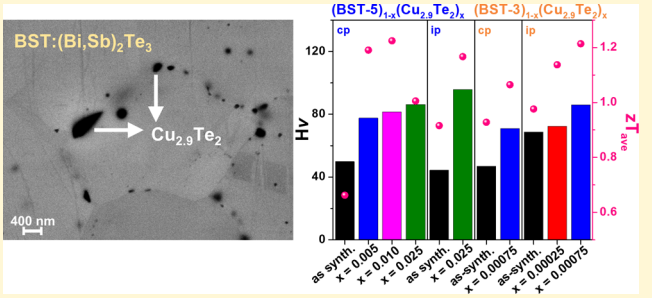

Downloaded via 78.112.186.107 on May 10, 2023 at 12:29:27 (UTC).
See https://pubs.acs.org/sharingguidelines for options on how to legitimately share published articles.

INTRODUCTION

The adverse outcomes of heavily utilized energy sources have motivated scientists to find out ways to recover waste heat reaching up to 70% for different sectors of end use.[1] Thermoelectric (TE) materials have attracted significant attention as a sustainable and clean energy source by converting waste heat into electricity and functioning as solid-state coolers.[2,3] However, their low conversion efficiency restrains their widespread applications. The efficiency of thermoelectric materials depends on the dimensionless thermoelectric figure of merit, zT, defined as $zT = \alpha^2\sigma T/(\kappa_{ph} + \kappa_{el})$, where α, σ, T, κ_{ph}, and κ_{el} are the Seebeck coefficient (or thermopower), electrical conductivity, absolute temperature, and lattice and electronic thermal conductivity, respectively.[4] Due to the interdependency of thermoelectric transport coefficients, maximizing the zT values of materials is extremely challenging.[5] Furthermore, for device applications, it is of great importance to obtain a high efficiency zT over a wide temperature range, instead of attaining a peak zT at a specific temperature.[6,7]

Bi$_2$Te$_3$-based alloys remain the best near-room-temperature thermoelectric materials and are widely used in Peltier coolers and low-grade power generation systems.[6,8−10] *p*-type Bi$_{0.5}$Sb$_{1.5}$Te$_3$ (BST) showed high and reproducible zT values of around 1.2 at 300 K,[11−13] while *n*-type Bi$_2$(Te, Se)$_3$ show lower zT values that fall below unity at 300 K.[14−19] High carrier mobility and band degeneracy along with intrinsically low lattice thermal conductivity of these materials allow for a high thermoelectric efficiency to be reached around room temperature. On the other hand, the low band gap of ∼0.15 eV for Bi$_2$Te$_3$ results in excitations of minority carriers that typically onset at 400 K, causing a dramatic reduction in the zT values at higher temperatures.[9,20]

Up to now, many different techniques have been applied to enhance the zT values of Bi$_2$Te$_3$-based alloys, including doping/alloying,[21−25] defect engineering,[8,26] nanostructuring,[27−29] or texturing.[30−32] Previous studies revealed that the peak zT values of Bi$_2$Te$_3$-based materials outreach 1.2 around 300 K for alloyed compositions and after applying complex synthesis procedures.[33−35] Commercial materials are usually synthesized in the form of single crystals or zone-melted ingots with a high degree of texture.[8,19,36] However, the high deformation texturing techniques applied during the synthesis lead to high production cost and poor mechanical stability of the materials.[16,32,37,38]

With recent studies introducing a second phase to the (Bi, Sb)$_2$Te$_3$ matrix through alloying or doping, peak zT values could be shifted toward higher temperatures.[39−44] Besides

Received: February 1, 2023
Revised: April 12, 2023
Published: April 25, 2023

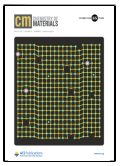

© 2023 The Authors. Published by American Chemical Society

enhanced thermoelectric properties, incorporating a phase with high mechanical strength, such as SiC or MgB_2, into the matrix improved the mechanical properties of $Bi_2(Te, Se)_3$[6,45] and $(Bi, Sb)_2Te_3$.[46] Moreover, doping $(Bi, Sb)_2Te_3$ with Ag, Pb, Cu, or Cd increased the hole concentration, thereby hindering the bipolar effect, but at the expense of reduced carrier mobility.[25,39−42,47] Among these elements, several studies were focused on Cu through direct doping or by adding a binary Cu-rich alloy.

Prominent examples of this last strategy notably include alloying Bi_2Te_3 with Cu_2Se nanostructures and $Bi_{0.3}Sb_{1.7}Te_3$ with Cu_2Te. In the first case, the presence of Cu resulted in forming Se_{Te} and Cu_{Bi} antisite defects leading to an enhanced power factor ($\alpha^2\sigma$). Meanwhile, the formation of Cu_7Te_5 (rickardite phase, described by another composition) as a secondary phase and localized Te-deficient regions were shown to act as hierarchical phonon scattering sources, yielding a substantial decrease in the lattice thermal conductivity.[48] Alloying $Bi_{0.3}Sb_{1.7}Te_3$ with Cu_2Te optimized the hole concentration through both Cu substitution and formation of intrinsic defects, which also contributed to lower the lattice thermal conductivity due to enhanced point defect scattering.[44] However, most of the alloys reported so far in literature do not show concomitantly enhanced mechanical properties and high average zT values.

In an attempt to overcome this issue, we investigated the influence of the Cu-rich rickardite mineral $Cu_{2.9}Te_2$ on the thermoelectric and mechanical properties of $(Bi, Sb)_2Te_3$ compounds. In addition to benefiting from the presence of Cu, directly alloying with a mineral can increase the time and cost efficiency of the fabrication process. Moreover, the incorporation of secondary phases with different chemical compositions in microstructures can facilitate the attainment of unique thermodynamic states, resulting in diverse defect concentrations that can ultimately enhance the optimization of thermoelectric properties.[47] Synthetic rickardite has been added to two distinct *p*-type alloys, $Bi_{0.5}Sb_{1.5}Te_3$ (BST-5) and $Bi_{0.3}Sb_{1.7}Te_3$ (BST-3), which exhibit different peak zT temperatures, a desirable characteristic to be implemented in segmented thermoelectric modules.[8] The incorporation of $Cu_{2.9}Te_2$ results in higher zT values between 400 and 550 K, ultimately reaching 1.32 at 467 K and 1.30 at 400 K in BST-5 and BST-3, respectively. Likewise, the microhardness of both samples is significantly enhanced, doubled for the BST-5 and increased 50% for the BST-3, respectively, compared to pristine BST. The improved thermoelectric performance and mechanical stability of these alloys demonstrated herein is of great relevance for large-scale applications of BST-based materials in conventional and segmented thermoelectric devices.

EXPERIMENTAL METHOD

Sample Preparation. $Bi_{0.5}Sb_{1.5}Te_3$ and $Bi_{0.3}Sb_{1.7}Te_3$ samples were prepared by solid-state synthesis with annealing and high energy ball milling, respectively. Raw materials of bismuth (Bi, Sigma-Aldrich >99.999% metals basis), antimony (Sb, Sigma-Aldrich >99.999% metals basis) shots, and tellurium pieces (Te, Sigma-Aldrich >99.999% metals basis) were used as starting materials to synthesize both compositions. Rickardite mineral, $Cu_{2.9}Te_2$, incorporated into BST medium was synthesized by following the same procedure described in our previous study.[49] To prepare the $Cu_{2.9}Te_2$ sample, elemental copper (Cu, Sigma-Aldrich 99.99% metal basis) and tellurium (Te, Alfa Aesar 99.999% metals basis) were reacted in a stoichiometric ratio by solid-state synthesis. The raw materials were sealed inside a carbon-coated fused silica tube under vacuum, which was then placed in a muffle furnace and held at 1223 K for 12 h. After quenching the tube in water at room temperature, the tube was placed back in the furnace for further annealing at 623 K for 4 days. For the preparation of $Bi_{0.5}Sb_{1.5}Te_3$, the raw materials were sealed into a fused silica tube under vacuum and transferred to a muffle furnace, where they were held at 1073 K for 10 h. To perform the mechanochemical treatment, the as-synthesized $Bi_{0.5}Sb_{1.5}Te_3$ was mixed with $Cu_{2.9}Te_2$ powder and loaded into a stainless-steel container inside an Ar-filled glovebox. The mixture was then ball-milled for 10 min. To prepare the $Cu_{2.9}Te_2$-incorporated $Bi_{0.3}Sb_{1.7}Te_3$ samples, stoichiometric amounts of Bi, Sb, and Te elements, along with the previously prepared $Cu_{2.9}Te_2$, were loaded into a stainless-steel vial and ball-milled for 90 min using high-energy ball milling.

Composite samples were prepared with the ratios varying between $x = 0-0.150$ for $(Bi_{0.5}Sb_{1.5}Te_3)_{1-x}(Cu_{2.9}Te_2)_x$ and $x = 0-0.005$ for $(Bi_{0.3}Sb_{1.7}Te_3)_{1-x}(Cu_{2.9}Te_2)_x$. The samples, labeled by their nominal stoichiometry, represent the undoped sample without ball-milling, while the $x = 0$ sample represents the ball-milled, undoped sample to determine the effect of ball milling on the transport properties. The obtained powders were loaded into a graphite die and consolidated by spark plasma sintering (SPS) for 10 min at 873 K under a pressure of 50 MPa. The dense 10 mm height cylindrical pellets were obtained for chemical characterizations and transport property measurements. The measured densities of the BST-5 samples fell within the range of 6.56−6.70 g/cm^3, which corresponds to relative densities of 97−99%. However, the as-synthesized BST-5 sample using the solid-state method without ball-milling had a density of 6.33 g/cm^3 with a relative density of 94%. For the BST-3 samples, the measured densities were in the range of 6.38 to 6.57 g/cm^3, with relative densities between 97 and 99% (Table S1).

Sample Characterization. The phase purity of samples was characterized by using a Rigaku MiniFlex 600 (Cu Kα = 1.5418 Å, 40 kV voltage, and 15 mA) and a Huber Guinier G670 camera (Cu Kα_1 radiation = 1.54056 Å). Lattice parameter calculations were performed with WinCSD program package.[50] Microstructure analyses of the samples were performed using scanning electron microscopy (SEM, Jeol JSM 7800F Field Emission cathode) equipped with an EDX system and optical microscopy (OM, Zeiss Axioplan 2) techniques and OM. The chemical compositions of the target phase were determined by electron microprobe analysis using wavelength-dispersive X-ray spectroscopy (WDS, Cameca SX 100, tungsten cathode). Atom-probe tomography (APT) studies were performed using a Cameca local-electrode atom-probe 4000X-Si tomograph. The micro array samples for the APT analysis were prepared by using focus ion beam (FIB) FEI Helios Nanolab 600 SEM/FIB dual beam system via the lift out method. Microhardness of the samples were measured by Shimadzu HMV-G Vickers Microhardness Tester by taking the average of 15 various spots with a load of 9.807 mN. Hv values were calculated according to the relation $Hv = 1.8544F_0/d^2$ where F_0 is the applied load and d is the diagonal length of indentation impression.

Transport Property Measurements. The SPS-consolidated pellets were cut into appropriate shapes with a diamond-wire saw for thermal and electrical transport measurements along cross-plane and in-plane directions. All measurements were performed between 323 and 523 K. Thermal diffusivity D measurements were carried out using a NETZSCH LFA HT467 laser flash apparatus. Thermal conductivities of samples were calculated using $\kappa = DC_pd$, where C_p is the Dulong-Petit heat capacity and d is the experimental density of the sample. Electrical conductivity and Seebeck coefficient measurements were carried out on bar-shaped samples using a four-probe method on a ZEM-3 measurement system (Ulvac-Riko, Japan). Hall coefficient measurements were performed by the Van der Pauw technique with a reversible magnetic field of 1 T using pressure-assisted tungsten electrodes. zT_{ave} values of the samples were calculated by using $zT_{ave} = \frac{\int_{Tc}^{Th} zT\,dT}{Th - Tc}$. The thermoelectric device figure of merit, ZT, and the maximum conversion efficiency, η_{max}, were calculated using the method reported by Snyder and Snyder.[51]

https://doi.org/10.1021/acs.chemmater.3c00229
Chem. Mater. 2023, 35, 3603−3613

RESULTS AND DISCUSSION

Crystal Structure and Phase Analysis. The rhombohedral crystal structure of $(Bi, Sb)_2Te_3$ is built up by quintuple layers with the sequence Te(1)-Bi-Te(2)-Bi-Te(1) (Figure 1a). In this structure, Te(1) layers are connected by weak Van der Waals interactions while Bi-Te octahedra are formed by strong covalent bonds.[5,36] This unique crystal structure induces strong anisotropy, which necessitates the measurement of in-plane (perpendicular to the pressing direction) and cross-plane (parallel to the pressing direction) transport properties. The synthetic rickardite mineral, $Cu_{3-x}Te_2$ ($x \leq 0.2$) crystallizes in an orthorhombic space group *Pmmn* (Figure 1b) at room temperature,[49] and undergoes phase transitions at higher temperatures (tetragonal above 473 K and presumably hexagonal above 673 K).[49] In the orthorhombic crystal structure of $Cu_{3-x}Te_2$, Cu atoms are distributed on two crystallographic sites, whereas Te atoms are located on one site. While the 2a site is fully occupied by Cu1 atoms, Cu2 atoms only partially occupy the 2b site. The Cu1-Te interaction creates a corrugated Cu1-Te framework accommodating the Cu2 atoms in the cavities. The tetragonal structure of rickardite, isotypic to Cu_2Sb, can be described in the *P4/nmm* space group with Cu1-Te layers weakly bounded to the Te atoms through partially filled Cu2 sites.

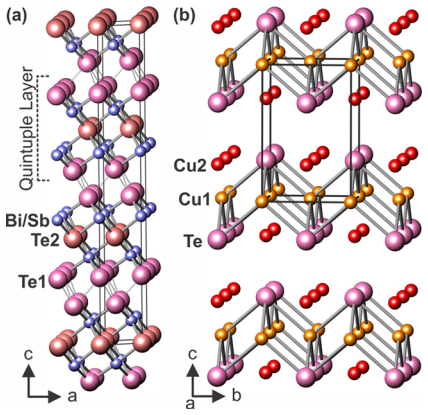

Figure 1. Crystal structures of (a) $(Bi, Sb)_2Te_3$ and (b) low-temperature orthorhombic phase of $Cu_{3-x}Te_2$.

The PXRD patterns of BST-5 and BST-3 samples show that the target $Bi_{0.5}Sb_{1.5}Te_3$ and $Bi_{0.3}Sb_{1.7}Te_3$ phases have been obtained successfully (Figure 2). Figure 2b shows that the most intense peaks of $Cu_{2.9}Te_2$ are only observed in BST-5 samples with a high percentage of addition. Due to its low concentration in the BST-3 matrix, there is no detectable $Cu_{2.9}Te_2$ peaks. The lattice parameter calculations indicate a slight decrease in the *a* value and a marginal increase in the *c* value for both BST-5 and BST-3 samples upon doping with $Cu_{2.9}Te_2$, as shown in Figure S1. Previous studies have observed that in the crystal structure of BST, Cu can either substitute on the Bi/Sb site,[5,42,44,47,52,53] or be intercalated in the van der Waals gaps located between quintuple layers.[54] If Cu is intercalated, then the *c* parameter should increase with the increase in Cu content. On the other hand, if Cu substitutes on the Bi/Sb site, the *a* parameter may decrease due to the difference in ionic radii between Cu^{1+} (91 pm, Shannon[55]) and Cu^{2+} (87 pm, Shannon) compared to Sb^{3+} (90 pm, Shannon) and Bi^{3+} (117 pm, Shannon). Our PXRD analyses indicate that both scenarios may occur simultaneously, with a small fraction of Cu being incorporated into the BST matrix.

Figures 3 and S2 show that the $Cu_{2.9}Te_2$ grains in the BST-5 and BST-3 microstructures decorate the grain boundaries almost homogeneously. $Cu_{2.9}Te_2$ grains are seen as dark spots in the microstructure, which can be differentiated by elemental mapping (Figure 4). The accurate compositions were obtained from WDS analysis by averaging 10 measured data points performed on the BST grains (Table S2). Even for the lowest doping level, Cu could be detected on the BST-5 sample with $x = 0.005$ as $Cu_{0.037(1)}Bi_{0.491(6)}Sb_{1.487(4)}Te_3$ in cross-plane and

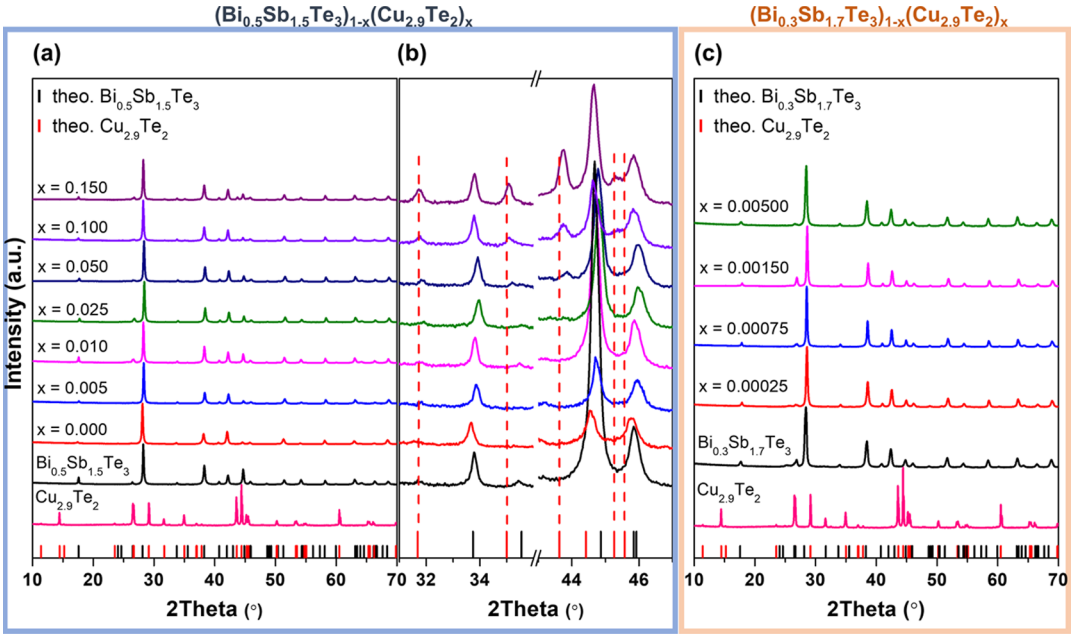

Figure 2. XRD patterns (Cu Kα) of (a) BST-5, (b) magnified region (2θ between 31 and 47°) shows $Cu_{2.9}Te_2$ and (c) BST-3 after SPS. The black and red ticks mark the theoretical peak positions of the $(Bi, Sb)_2Te_3$ phases and orthorhombic phase of $Cu_{2.9}Te_2$, respectively.

https://doi.org/10.1021/acs.chemmater.3c00229
Chem. Mater. 2023, 35, 3603−3613

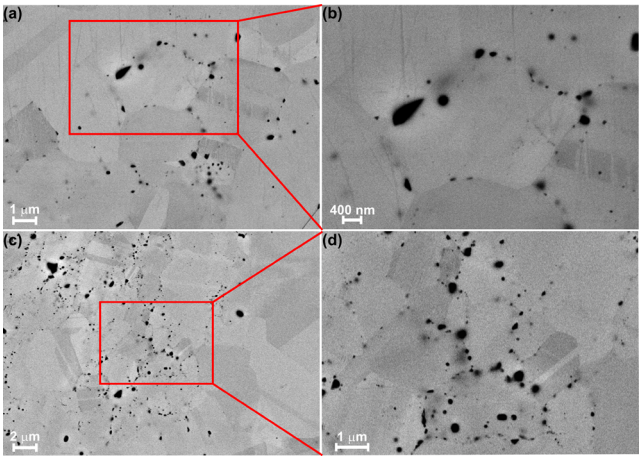

Figure 3. BSE (back-scattered electron) images (20 kV HV) of the BST-5 sample with x = 0.005: (a,b) cross-plane and (c,d) in-plane direction.

$Cu_{0.037(1)}Bi_{0.493(5)}Sb_{1.478(4)}Te_3$ in in-plane directions, indicating that a small amount of Cu was incorporated into the crystal structure of the main phase. On the other hand, it was not possible to detect Cu on the BST-3 sample with x = 0.00075 as this level of doping is below the detection limit of WDS. The compositions of the main phases were found to be close to the nominal compositions of $Bi_{0.5}Sb_{1.5}Te_3$ and $Bi_{0.3}Sb_{1.7}Te_3$, respectively, with only slight variations of Bi and Sb content among the measured points.

To determine the distribution of elements and Cu localization at the atomic scale, APT was utilized. Due to the ease of erosion of the tip by ion milling during shaping, isolating the BST/CuTe grain boundary proved difficult even after multiple attempts. Despite this, the obtained microarray was found to be in close proximity to a grain boundary to a rickardite region. Figure 5a displays the 3D reconstructed APT data, containing 60 million atoms, with a 10% fraction display. Figure 5b presents the compositional line profile of Bi, Sb, and Te atoms from the selected cylinder (C2) volume, indicating a small degree of compositional inhomogeneity in the Bi and Sb contents, as reported in prior studies.[56] The presence of Cu in the microarray in the BST grain can be identified by examining the mass-to-charge ratio spectrum (Figure S3a) of the sample and focusing on Cu^+ isotope regions (Figure S3b). However, due to the overlap of mass-to-charge values of Te^{2+} isotopes of 126 and 130 with Cu^+ isotopes of 63 and 65, the quantitative determination of Cu inclusion in the BST region is not possible. Nevertheless, the intensity difference between these lines provides evidence of Cu inclusion in the grain. The atoms are assigned together based on the mass-to-charge ratio values of 63, 64, and 65, and Figure S3c presents the 3D reconstructed APT data from the selected cylinder (C1) volume of the first 15 million atoms of the microarray, in which the assigned atoms make up less than 1% of the ionic concentration. In addition to APT data obtained from very limited area of the sample, the existence of Cu and compositional fluctuation with respect to Bi, Sb, and Te content were observed using EDS line scan analysis for the main grains and the grain boundaries (Figure S4).

As reported previously for polycrystalline $Cu_{2.9}Te_2$, the strong orientation contrast in polarized light helps to locate the phase throughout the BST matrix.[49] Figures S5 and S6 show the polarized optical micrographs of the BST-5 sample with x = 0.005 and x = 0.025, respectively. The rickardite phase is clearly visible and is in contact with some large and small micron-sized grains of the BST phase. As shown in Figure 6, in the in-plane direction of the BST-5 sample with x = 0.005, the BST grains show a plate-like morphology and are thus highly oriented while this texture is less obvious along the cross-plane direction. This feature was found to be more pronounced for the x = 0.025 composition (Figure S7). The anisotropic crystal structure along with solid-state synthesis with long annealing

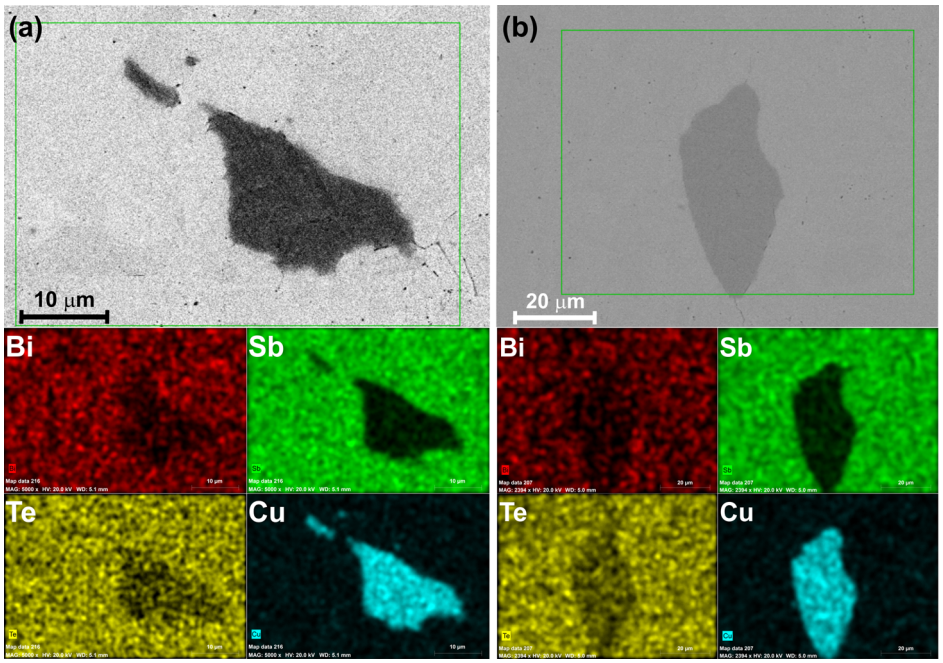

Figure 4. SE (secondary electron) images (20 kV HV) of the BST-5 sample with x = 0.005: (a) cross-plane and (b) in-plane direction with elemental mappings of Bi, Sb, Te, and Cu.

https://doi.org/10.1021/acs.chemmater.3c00229
Chem. Mater. 2023, 35, 3603−3613

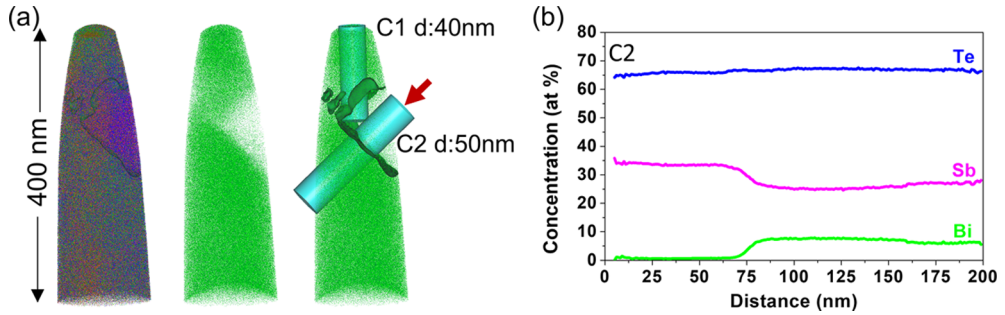

Figure 5. (a) 3D atom maps of elemental fractions and Bi (green) by APT analysis and (b) composition line profile of constituent elements calculated from selected cylinder volume in atom maps of Bi obtained from BST-3 with x = 0.00075 sample, indicating some inhomogeneity of Bi and Sb distributions in the grains of the BST phase.

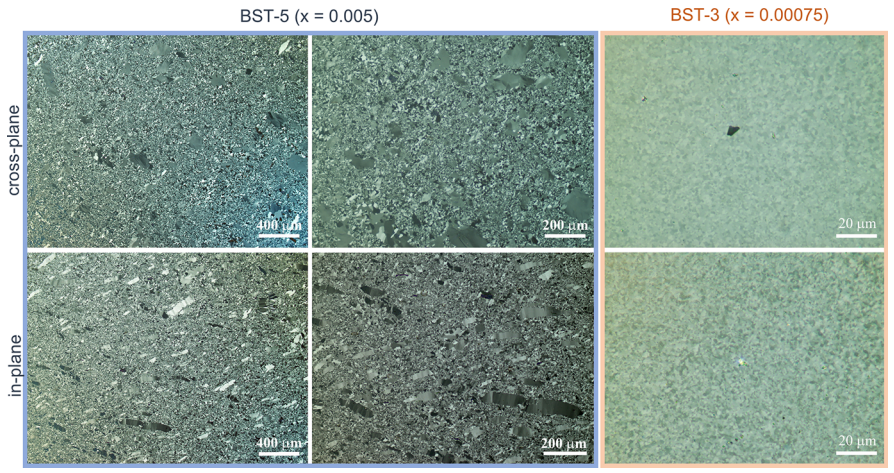

Figure 6. OM images of the BST-5 sample with x = 0.005 and BST-3 sample with x = 0.00075: top ones along the cross-plane and bottom ones along the in-plane direction, indicating the preferred orientation of the BST grains along the in-plane direction for BST-5 but not for BST-3.

times at relatively high temperatures, may facilitate the formation of such oriented grains.

For the BST-3-based samples, the rickardite phase is less easily detectable by SEM because of the minute amount of $Cu_{2.9}Te_2$ in these samples. On the other hand, polarized OM images of $(Bi_{0.3}Sb_{1.7}Te_3)_{0.99925}(Cu_{2.9}Te_2)_{0.00075}$ present some shiny orange particles like those observed in $(Bi_{0.5}Sb_{1.5}Te_3)_{0.995}(Cu_{2.9}Te_2)_{0.005}$ and can be thus safely attributed to $Cu_{2.9}Te_2$ (Figure 6). In terms of grain size and nature of the preferred orientation, the microstructure indicates very different features compared to the BST-5 samples. First, the grain sizes are found to be very small (submicron) and more homogeneous throughout the microstructure. Additionally, no preferred orientation is observed in either direction due to the synthetic route followed for preparing the BST-3 samples relying on high-energy ball milling.

Transport Properties. *Thermoelectric Transport Properties of* $(Bi_{0.5}Sb_{1.5}Te_3)_{1-x}(Cu_{2.9}Te_2)_x$. The electronic properties of Bi_2Te_3-based alloys are governed by their defect chemistry.[9] In the binary compound Bi_2Te_3, both Bi_{Te} antisite defect (contributing one hole per defect), due to the small difference in electronegativity between Bi (2.02, Pauling scale) and Te (2.10, Pauling scale), and Te vacancies (contributing two electrons per defect) are the main types of defects. The former is mainly responsible for the intrinsic p-type properties observed in most single crystals and large-grain polycrystals.[9] Upon alloying Bi_2Te_3 with Sb_2Te_3, the substitution of Sb for Bi tips the balance between both types of defects toward antisite defects due to the smaller difference in electronegativity between Sb (2.05) and Te (2.10) compared to Bi (2.02) and Te (2.10). Thus, in Sb-rich compositions, such as $Bi_{0.5}Sb_{1.5}Te_3$ considered herein, degenerate p-type electronic properties are expected. The transport properties of the $(Bi_{0.5}Sb_{1.5}Te_3)_{1-x}(Cu_{2.9}Te_2)_x$ samples along the cross-plane direction are consistent with these expectations for pristine samples (Figure 7), with an electrical conductivity σ decreasing with the increase in temperature and positive Seebeck coefficients S. These measurements further evidence the direct role of rickardite in tuning the thermoelectric performance of BST. σ gradually increases with the increase in x from 500 S cm^{-1} in BST up to 3000 S cm^{-1} for x = 0.15. For all doped samples, the trend in $\sigma(T)$ with the increase in temperature is indicative of a degenerate semiconducting nature. The increased metallic character of transport is further reflected by the magnitude of S, which decreases with the increase in x. The maximum in S reached near 350 K in the pristine BST sample signals the beginning of the intrinsic regime of conduction characterized by excitation of minority carriers across the electronic band gap.

The trend observed in the electronic transport can be explained by the dissolution of a small fraction of Cu into the BST matrix evidenced by APT and WDS analyses. Assuming that Cu mainly substitutes for Bi/Sb, the distinct valence state of Cu with fewer electrons with respect to Sb is expected to give rise to enhanced hole concentrations in doped samples.

https://doi.org/10.1021/acs.chemmater.3c00229
Chem. Mater. 2023, 35, 3603−3613

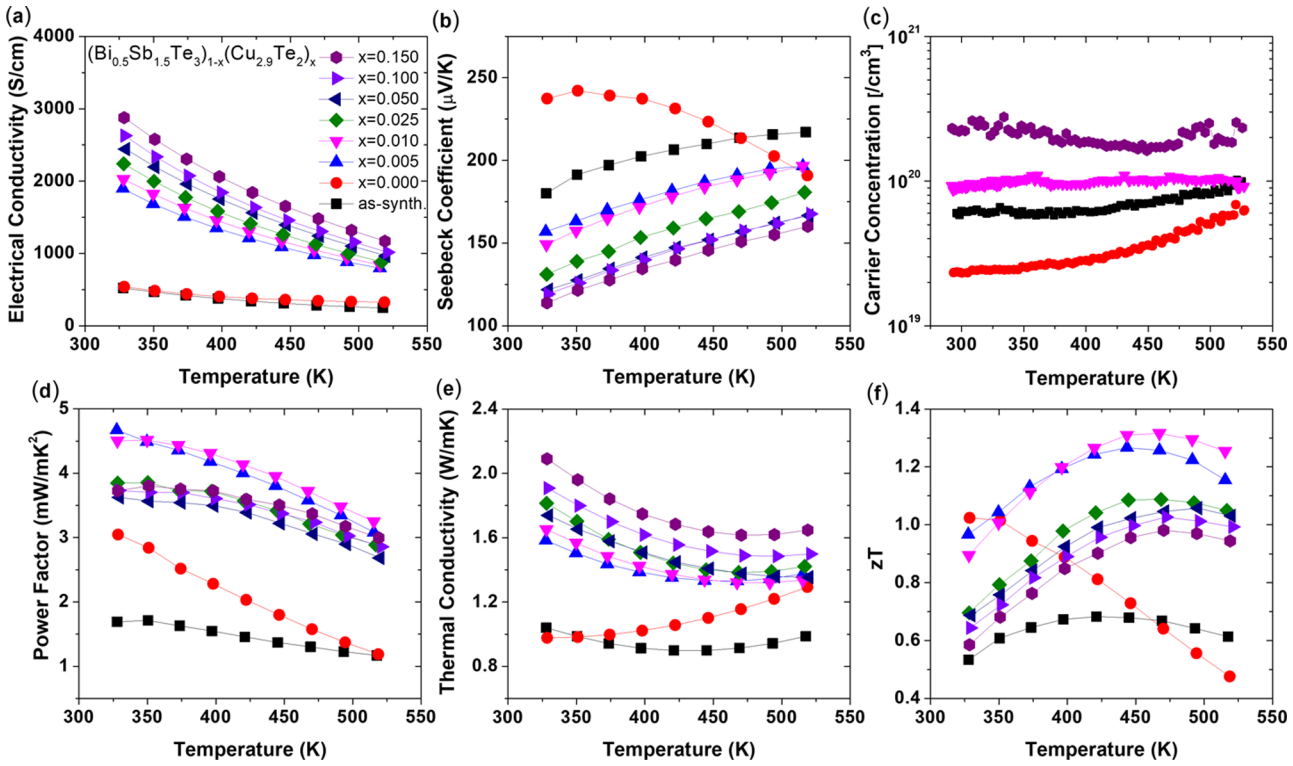

Figure 7. Temperature-dependent thermoelectric transport properties of $(Bi_{0.5}Sb_{1.5}Te_3)_{1-x}(Cu_{2.9}Te_2)_x$ samples through the cross-plane direction. (a) Electrical conductivity, (b) Seebeck coefficient, (c) power factor, (d) carrier concentration, (e) thermal conductivity, and (f) dimensionless thermoelectric figure of merit, zT.

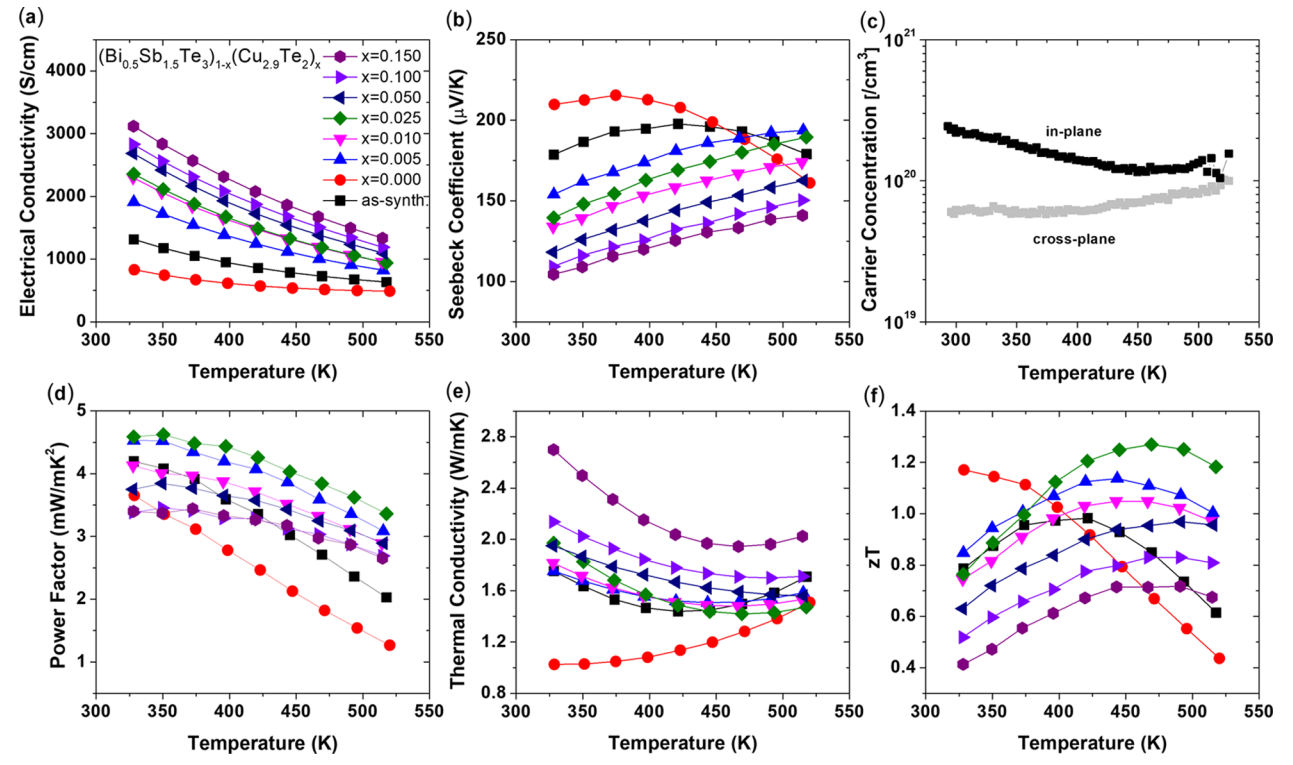

Figure 8. Temperature-dependent thermoelectric transport properties of $(Bi_{0.5}Sb_{1.5}Te_3)_{1-x}(Cu_{2.9}Te_2)_x$ samples through the in-plane direction. (a) Electrical conductivity, (b) Seebeck coefficient, (c) power factor, (d) carrier concentration, (e) thermal conductivity, and (f) dimensionless thermoelectric figure of merit, zT.

This doping mechanism is supported by the Hall carrier concentration trends indicative of higher hole concentrations attained with increasing x (Figure 7c). We note that 10 min of high-energy ball milling without $Cu_{2.9}Te_2$ addition led to lower

https://doi.org/10.1021/acs.chemmater.3c00229
Chem. Mater. 2023, 35, 3603−3613

hole concentrations due to the formation of intrinsic donor-like defects as previously discussed.[57] The temperature-dependent Hall mobility $\mu_H = 1/(n_H e\rho)$ data, shown in Figure S8a, imply acoustic phonon scattering as the prominent scattering mechanism. All these results are consistent with the intrinsic regime, reached above 350 K in the BST sample, being shifted toward higher temperatures in doped samples. Maximum power factor values are achieved for both $x = 0.005$ and 0.010 in the BST-5 samples (Figure 7d).

Figure 7e shows the temperature dependence of the total thermal conductivity κ, which is the sum of an electronic contribution due to charge carriers κ_e, a lattice contribution κ_l, and a bipolar contribution due to minority carriers κ_b. The slight upturn in κ observed at 450 K in BST reflects this last contribution, which is suppressed upon incorporating increasing amounts of $Cu_{2.9}Te_2$. κ_e has been estimated by the Wiedemann–Franz law $\kappa_e = L\sigma T$, where L is the Lorenz number calculated through the relation $\frac{L}{10^{-8}\,\mathrm{W\Omega\,K^{-2}}} = 1.5 + \exp\left(\frac{-|\alpha|}{116\,\mu\mathrm{V/K}}\right)$.[58] In doped samples, the lattice thermal conductivity κ_l is lowered, an effect that can be ascribed to enhanced phonon scattering resulting from the presence of $Cu_{2.9}Te_2$.

The combination of improved power factor and lowered phonon transport upon adding rickardite leads to a significant increase in the zT values (Figure 7f). Although the room-temperature value is nearly similar for $x = 0.005$ and 0.010, their medium-temperature zT reaches a peak value of 1.32, which is among the highest values reported for doping studies on BST-5.[59,60] The shift in the temperature at which this maximum occurs is a direct consequence of the suppression of the bipolar contribution to S. More importantly, the zT values plateau between 425 and 525 K giving rise to an improved average zT of 1.22, which is an essential requirement for designing thermoelectric modules with enhanced device efficiency.

In the in-plane direction of BST-5 samples, the electronic and thermal transport behaviors are parallel to those observed along the cross-plane direction (Figures 8 and S9). The electrical conductivity in the pristine compound is almost twice as high as along the cross-plane direction due to its higher carrier concentration as depicted in Figure 8a,c. In addition to higher carrier concentration, preferred orientation of the BST grains along the in-plane direction may contribute to that further (see Figure 6). The 10 min ball-milled sample without $Cu_{2.9}Te_2$ shows slightly lower electrical conductivity and higher Seebeck coefficient compared to the as-synthesized material. This is consistent with the reduced concentration of p-type defects due to the ball-milling process.[61] The highest power factor is achieved for the $x = 0.05$ sample. As x increases, the thermal conductivity increases similar to the cross-plane direction. Room-temperature zT value was the highest for the 10 min ball-milled sample without $Cu_{2.9}Te_2$. However, at temperatures above 400 K, the zT value of this sample considerably drops down due to minority carrier activation. The $x = 0.05$ sample attained the highest zT of ca. 1.3 at 475 K thanks to its highest power factor and lowest κ_l values.

Thermoelectric Transport Properties of $(Bi_{0.3}Sb_{1.7}Te_3)_{1-x}(Cu_{2.9}Te_2)_x$. The beneficial influence of rickardite on the peak and average zT is further demonstrated in the series $(Bi_{0.3}Sb_{1.7}Te_3)_{1-x}(Cu_{2.9}Te_2)_x$ with $x = 0$, 0.00025, 0.00075, 0.0015, and 0.005 in which both quantities are also improved (Figures S10 and S11). Similar to the results obtained in BST-5, rickardite incorporation increases the zT of BST-3 along the in-plane direction up to a maximum value of 1.27 for $x = 0.00075$. For these samples, the suppression of bipolar conduction is also observed in the thermal conductivities of doped samples which have a linear decreasing trend with temperature. In addition to increasing the peak zT, $Cu_{2.9}Te_2$ addition shifts the temperature, where the zT values plateau to around 400 K. On the other hand, $Cu_{2.9}Te_2$ incorporation through the cross-plane direction causes a stepwise increment in the value and temperature of plateau zT. Benefiting from these increased zT values, a module design with a segmented single p-type leg is proposed for both thermoelectric power generation and Peltier cooling (Figure 9). The p-type leg is composed of BST-3 and BST-5 cross-plane samples with $x = 0.00025$ and 0.010, respectively, to achieve device ZT values of 0.95–1.15 in the temperature range 323–523 K. η_{max} reaches 7% at 525 K,[51,62,63] which is a very competitive value for compositionally segmented $Bi_xSb_yTe_3$ tri-block thermoelectric leg.[64]

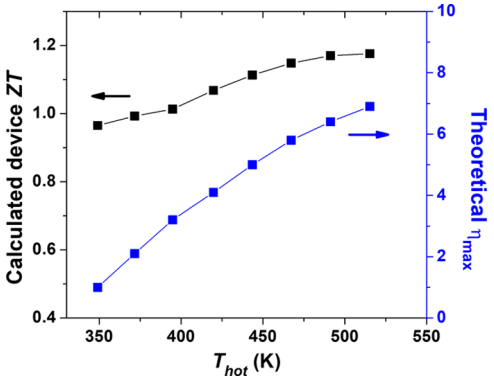

Figure 9. Calculated device ZT and theoretical device efficiency of $(Bi, Sb)_2Te_3/Cu_{2.9}Te_2$ composite combinations of the best BST-3 and BST-5 cross-plane samples with $x = 0.00025$ and 0.010, respectively.

Vickers Microhardness Test. Although BST compounds usually exhibit zT values close to unity, their mechanical instability makes their integration into micro-devices challenging. As illustrated in Figure 10, compared with other BST alloys, rickardite incorporation into the BST matrix is found to be very promising for improving the mechanical stability of both BST-5 and BST-3 and, concomitantly, their average figure of merit (zT_{ave}). Vickers microhardness values increase with the increase in $Cu_{2.9}Te_2$ content for both BST-5 and BST-3 samples and for both directions, with the utmost enhancement being about 116 and 51% for BST-5 and BST-3, respectively.

The values of $(Bi_{0.5}Sb_{1.5}Te_3)_{0.975}(Cu_{2.9}Te_2)_{0.025}$ reach up to 86.28 Hν and 95.86 Hν in cross-plane and in-plane direction, respectively, which is significantly higher compared to other BST samples synthesized by solid-state synthesis and commercially available zone-melted (ZM) BST-5.[71] The zT_{ave} values of the samples were calculated between 350 and 500 K to compare with literature data usually reporting them within this range. Considering their zT_{ave} and hardness, the best BST-5 samples would be for $x = 0.010$ for cross-plane with 81.55 Hν and 1.22 zT_{ave}, while it would be $x = 0.025$ for in-plane with 95.86 Hν and 1.17 zT_{ave}. The best BST-3 sample would be $x = 0.00075$ with zT_{ave} of 1.06 and 70.89 Hν for cross-plane and zT_{ave} of 1.21 and 85.99 Hν for in-plane direction. These values are slightly higher than those reported

https://doi.org/10.1021/acs.chemmater.3c00229
Chem. Mater. 2023, 35, 3603–3613

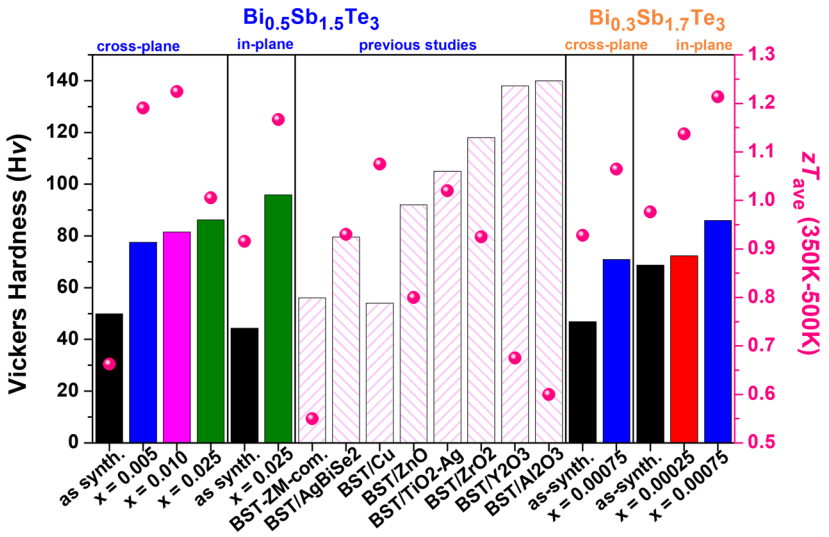

Figure 10. Vickers microhardness (Hv) values for $(Bi_{0.5}Sb_{1.5}Te_3)_{1-x}(Cu_{2.9}Te_2)_x$ and $(Bi_{0.3}Sb_{1.7}Te_3)_{1-x}(Cu_{2.9}Te_2)_x$ along cross-plane and in-plane directions. Experimental data from the literature are shown for comparison.[65−70] (ZM: zone melted, commercial) The pink filled circles stand for the corresponding zT_{ave} values calculated in the temperature range 350−500 K.

for BST-3/Cu_2Te with $zT_{ave} \sim 1.12$.[44] The commercial BST (BST-ZM-com.) grown by zone-melted method has zT_{ave} below 0.6 with 50 Hν, that is, low zT_{ave} and poor mechanical stability compared to pristine BST-5 sample in this work.[65] Previous studies on BST alloys reporting transport properties along with mechanical properties generally resulted in deteriorated zT_{ave} values when the mechanical stability of the samples was enhanced (Figure 10).[66−70] The enhancement in Hν values achieved herein may be the consequence of diffusion of Cu ions into the BST grains or possibly in the BST interlayer, thereby forming defects that contribute to prevent the propagation of dislocations.

CONCLUSIONS

By incorporating a synthetic mineral, rickardite, into the state-of-the-art thermoelectric material $(Bi, Sb)_2Te_3$, we have shown how the peak and average figure of merit values can be optimized without being at the expense of good mechanical properties. Although thermoelectric transport properties of rickardite are poor at temperatures in which $(Bi, Sb)_2Te_3$ alloys are commonly used, the presence of $Cu_{3-x}Te_2$ induces doping of the main phase and additional scattering centers at the grain boundaries, drastically enhancing both transport and mechanical properties of $(Bi, Sb)_2Te_3$. These results were achieved in two distinct compositions, namely, $Bi_{0.5}Sb_{1.5}Te_3$ and $Bi_{0.3}Sb_{1.7}Te_3$. Incorporating $Cu_{2.9}Te_2$ into BST-5 enhances the zT by ca. 90%, reaching 1.32 at 500 K along the cross-plane direction, while the plateau zT is shifted toward higher temperatures and higher values simultaneously in the in-plane direction. Meanwhile, mechanical properties are also enhanced by 73 and 116% for cross- and in-plane directions, respectively. Similar results are obtained for the alloy $Bi_{0.3}Sb_{1.7}Te_3$, for which the zT values increase to 0.95 and 1.15 at 325 and 525 K, respectively. These results make these optimized materials attractive for a segmented module comprising rickardite-doped BST-3 and BST-5 in the *p*-type leg, with a maximum device ZT of around 1.15 at 523 K, along with a device efficiency of 7%. Overall, rickardite incorporation in BST alloys is a very promising route for achieving high thermoelectric efficiency and mechanical stability.

ASSOCIATED CONTENT

Supporting Information

The Supporting Information is available free of charge at https://pubs.acs.org/doi/10.1021/acs.chemmater.3c00229.

Lattice parameters of the samples; density measurements; BSE (back-scattered electrons) images; WDS analysis results; atom probe analysis results; EDS line scan images; polarized OM images; and temperature-dependent thermoelectric transport (PDF)

AUTHOR INFORMATION

Corresponding Author

Umut Aydemir − *Koç University Boron and Advanced Materials Application and Research Center (KUBAM), Istanbul 34450, Turkey; Department of Chemistry, Koç University, Istanbul 34450, Turkey;* orcid.org/0000-0003-1164-1973; Email: uaydemir@ku.edu.tr

Authors

Kivanc Saglik − *Graduate School of Sciences and Engineering, Koç University, Istanbul 34450, Turkey; Koç University Boron and Advanced Materials Application and Research Center (KUBAM), Istanbul 34450, Turkey*

Mujde Yahyaoglu − *Graduate School of Sciences and Engineering, Koç University, Istanbul 34450, Turkey; Koç University Boron and Advanced Materials Application and Research Center (KUBAM), Istanbul 34450, Turkey;* orcid.org/0000-0001-9098-2869

Christophe Candolfi − *Institut Jean Lamour, Université de Lorraine, Nancy Cedex 54011, France*

Complete contact information is available at: https://pubs.acs.org/10.1021/acs.chemmater.3c00229

Author Contributions

K.S. and M.Y. contributed equally. The manuscript was written through contributions of all authors. All authors have given approval to the final version of the manuscript.

https://doi.org/10.1021/acs.chemmater.3c00229
Chem. Mater. 2023, 35, 3603−3613

Funding

This work was supported by the Scientific and Technological Research Council of Turkey (TUBITAK) with project number 218M335. U.A. and C.C. acknowledge the financial support of the French Agence Nationale de la Recherche (ANR), through the PRCI project DENZIP (ANR-18-CE05-0042).

Notes

The authors declare no competing financial interest.

■ ACKNOWLEDGMENTS

We would like to thank Dr. Ulrich Burkhardt from Max Planck Institute for Chemical Physics of Solids, Dresden, Germany, for the WDS measurements. We acknowledge Barış Yağcı and other researchers at Koç University Surface Science and Technology Center (KUYTAM) for SEM measurements.

■ REFERENCES

(1) Forman, C.; Muritala, I. K.; Pardemann, R.; Meyer, B. Estimating the global waste heat potential. *Renew. Sustain. Energy Rev.* **2016**, *57*, 1568−1579.
(2) He, J.; Tritt, T. M. Advances in thermoelectric materials research: Looking back and moving forward. *Science* **2017**, *357*, No. eaak9997.
(3) Liu, H.; Shi, X.; Xu, F.; Zhang, L.; Zhang, W.; Chen, L.; Li, Q.; Uher, C.; Day, T.; Snyder, G. J. Copper ion liquid-like thermoelectrics. *Nat. Mater.* **2012**, *11*, 422−425.
(4) Snyder, G. J.; Toberer, E. S. Complex thermoelectric materials. *Nat. Mater.* **2008**, *7*, 105−114.
(5) Zhu, W.; Hu, W.; Wei, P.; Nie, X.; Zhao, W. Preparation and Enhanced Thermoelectric Properties of Cu/Bi 0.5 Sb 1.5 Te 3 Composite Materials. *J. Electron. Mater.* **2020**, *49*, 2962−2967.
(6) Pan, Y.; Aydemir, U.; Sun, F. H.; Wu, C. F.; Chasapis, T. C.; Snyder, G. J.; Li, J. F. Self-Tuning n-Type Bi2 (Te, Se) 3/SiC Thermoelectric Nanocomposites to Realize High Performances up to 300° C. *Adv. Sci.* **2017**, *4*, 1700259.
(7) Zheng, Y.; Slade, T. J.; Hu, L.; Tan, X. Y.; Luo, Y.; Luo, Z.-Z.; Xu, J.; Yan, Q.; Kanatzidis, M. G. Defect engineering in thermoelectric materials: what have we learned? *Chem. Soc. Rev.* **2021**, *50*, 9022−9054.
(8) Pan, Y.; Aydemir, U.; Grovogui, J. A.; Witting, I. T.; Hanus, R.; Xu, Y.; Wu, J.; Wu, C. F.; Sun, F. H.; Zhuang, H. L.; et al. Melt-centrifuged (Bi, Sb) 2Te3: engineering microstructure toward high thermoelectric efficiency. *Adv. Mater.* **2018**, *30*, 1802016.
(9) Witting, I. T.; Chasapis, T. C.; Ricci, F.; Peters, M.; Heinz, N. A.; Hautier, G.; Snyder, G. J. The thermoelectric properties of bismuth telluride. *Adv. Electron. Mater.* **2019**, *5*, 1800904.
(10) Hegde, G. S.; Parol, V.; Rao, A.; Prabhu, A.; Levinsky, J. J.; Blake, G. R. Thermoelectric properties of co-doped (Bi0. 98In0. 02) 2Te2. 7Se0. 3/reduced graphene oxide composites prepared by solid-state reaction. *Mater. Res. Bull.* **2022**, *145*, 111517.
(11) Zhuang, H.-L.; Pei, J.; Cai, B.; Dong, J.; Hu, H.; Sun, F.-H.; Pan, Y.; Snyder, G. J.; Li, J.-F. Thermoelectric Performance Enhancement in BiSbTe Alloy by Microstructure Modulation via Cyclic Spark Plasma Sintering with Liquid Phase. *Adv. Funct. Mater.* **2021**, *31*, 2009681.
(12) Wang, H.; Wu, G.; Yan, Z.; Tan, X.; Cai, J.; Hu, H.; Sun, P.; Liu, G.; Jiang, J. Synergistic effects of B-In codoping in zone-melted Bi0.48Sb1.52Te3-based thermoelectric. *Chem. Eng. J.* **2021**, *420*, 130381.
(13) El-Makaty, F. M.; Ahmed, H. K.; Youssef, K. M. Review: The effect of different nanofiller materials on the thermoelectric behavior of bismuth telluride. *Mater. Des.* **2021**, *209*, 109974.
(14) Poudel, B.; Hao, Q.; Ma, Y.; Lan, Y.; Minnich, A.; Yu, B.; Yan, X.; Wang, D.; Muto, A.; Vashaee, D.; et al. High-thermoelectric performance of nanostructured bismuth antimony telluride bulk alloys. *Science* **2008**, *320*, 634−638.
(15) Cope, R.; Penn, A. The powder metallurgy of n-type Bi 2 Te 2.55 Se 0.45 thermoelectric material. *J. Mater. Sci.* **1968**, *3*, 103−109.
(16) Yan, X.; Poudel, B.; Ma, Y.; Liu, W.; Joshi, G.; Wang, H.; Lan, Y.; Wang, D.; Chen, G.; Ren, Z. Experimental studies on anisotropic thermoelectric properties and structures of n-type Bi2Te2. 7Se0. 3. *Nano Lett.* **2010**, *10*, 3373−3378.
(17) Seo, J.; Cho, D.; Park, K.; Lee, C. Fabrication and thermoelectric properties of p-type Bi0. 5Sb1. 5Te3 compounds by ingot extrusion. *Mater. Res. Bull.* **2000**, *35*, 2157−2163.
(18) Hu, L.-P.; Zhu, T.-J.; Wang, Y.-G.; Xie, H.-H.; Xu, Z.-J.; Zhao, X.-B. Shifting up the optimum figure of merit of p-type bismuth telluride-based thermoelectric materials for power generation by suppressing intrinsic conduction. *NPG Asia Mater.* **2014**, *6*, No. e88.
(19) Suh, D.; Lee, S.; Mun, H.; Park, S.-H.; Lee, K. H.; Wng Kim, S.; Choi, J.-Y.; Baik, S. Enhanced thermoelectric performance of Bi0. 5Sb1. 5Te3-expanded graphene composites by simultaneous modulation of electronic and thermal carrier transport. *Nano Energy* **2015**, *13*, 67−76.
(20) Mishra, S.; Satpathy, S.; Jepsen, O. Electronic structure and thermoelectric properties of bismuth telluride and bismuth selenide. *J. Phys.: Condens. Matter* **1997**, *9*, 461−470.
(21) Hu, Q.; Qiu, W.; Chen, L.; Chen, J.; Yang, L.; Tang, J. Realize High Thermoelectric Properties in n-Type Bi2Te2. 7Se0. 3/Y2O3 Nanocomposites by Constructing Heterointerfaces. *ACS Appl. Mater. Interfaces* **2021**, *13*, 38526−38533.
(22) Yang, G.; Sang, L.; Mitchell, D. R.; Fei Yun, F.; Wai See, K.; Jumlat Ahmed, A.; Sayyar, S.; Bake, A.; Liu, P.; Chen, L.; et al. Enhanced thermoelectric performance and mechanical strength of n-type BiTeSe materials produced via a composite strategy. *Chem. Eng. J.* **2022**, *428*, 131205.
(23) Zhang, R.; Pei, J.; Shan, Z.; Zhou, W.; Wu, Y.; Han, Z.; Zhao, Y.-H.; Li, J.-F.; Ge, Z.-H.; Zhang, B.-P. Intrinsic vacancy suppression and band convergence to enhance thermoelectric performance of (Ge, Bi, Sb) Te crystals. *Chem. Eng. J.* **2022**, *429*, 132275.
(24) Deng, M.; Huang, Y. RETRACTED: Dispersing Bi2Mo2O9 nanoparticles into Bi0.5Sb1.5Te3 alloys for enhanced thermoelectric figure of merit (ZT) through phonon scattering. *Ceram. Int.* **2019**, *45*, 24914−24918.
(25) Wei, Z.; Li, Z.; Luo, P.; Zhang, J.; Luo, J. Simultaneously increased carrier concentration and mobility in p-type Bi0. 5Sb1. 5Te3 throng Cd doping. *J. Alloys Compd.* **2020**, *830*, 154625.
(26) Kim, S. I.; Lee, K. H.; Mun, H. A.; Kim, H. S.; Hwang, S. W.; Roh, J. W.; Yang, D. J.; Shin, W. H.; Li, X. S.; Lee, Y. H.; Snyder, G. J.; Kim, S. W. Dense dislocation arrays embedded in grain boundaries for high-performance bulk thermoelectrics. *Science* **2015**, *348*, 109−114.
(27) Hong, M.; Chen, Z.-G.; Yang, L.; Zou, J. Enhancing thermoelectric performance of Bi2Te3-based nanostructures through rational structure design. *Nanoscale* **2016**, *8*, 8681−8686.
(28) Yang, L.; Chen, Z. G.; Hong, M.; Han, G.; Zou, J. Enhanced Thermoelectric Performance of Nanostructured Bi2Te3 through Significant Phonon Scattering. *ACS Appl. Mater. Interfaces* **2015**, *7*, 23694−23699.
(29) Poudel, B.; Hao, Q.; Ma, Y.; Lan, Y. C.; Minnich, A.; Yu, B.; Yan, X. A.; Wang, D. Z.; Muto, A.; Vashaee, D.; Chen, X. Y.; Liu, J. M.; Dresselhaus, M. S.; Chen, G.; Ren, Z. F. High-thermoelectric performance of nanostructured bismuth antimony telluride bulk alloys. *Science* **2008**, *320*, 634−638.
(30) Hu, L.; Wu, H.; Zhu, T.; Fu, C.; He, J.; Ying, P.; Zhao, X. Tuning multiscale microstructures to enhance thermoelectric performance of n-type Bismuth-Telluride-based solid solutions. *Adv. Energy Mater.* **2015**, *5*, 1500411.
(31) Liu, Y.; Zhang, Y.; Lim, K. H.; Ibáñez, M.; Ortega, S.; Li, M.; David, J.; Martí-Sánchez, S.; Ng, K. M.; Arbiol, J.; et al. High Thermoelectric Performance in Crystallographically Textured n-Type $Bi_2Te_{3-x}Se_x$ Produced from Asymmetric Colloidal Nanocrystals. *ACS Nano* **2018**, *12*, 7174−7184.
(32) Wu, Y.; Yu, Y.; Zhang, Q.; Zhu, T.; Zhai, R.; Zhao, X. Liquid-Phase Hot Deformation to Enhance Thermoelectric Performance of

https://doi.org/10.1021/acs.chemmater.3c00229
Chem. Mater. 2023, 35, 3603−3613

n-type Bismuth-Telluride-Based Solid Solutions. *Adv. Sci.* **2019**, *6*, 1901702.
(33) Nguyen, P.; Lee, K.; Moon, J.; Kim, S. I.; Ahn, K.; Chen, L.; Lee, S.; Chen, R.; Jin, S.; Berkowitz, A. Spark erosion: a high production rate method for producing Bi0. 5Sb1. 5Te3 nanoparticles with enhanced thermoelectric performance. *Nanotechnology* **2012**, *23*, 415604.
(34) Wang, Z.; Vemishetti, A.; Ejembi, J. I.; Wei, G.; Zhang, B.; Wang, L.; Zhang, Y.; Guo, S.; Luo, J.; Chepko, C.; et al. High thermoelectric performance of fullerene doped Bi0. 5Sb1. 5Te3 alloys. *Mater. Sci. Eng., B* **2016**, *205*, 36−39.
(35) Kim, S. I.; Lee, K. H.; Mun, H. A.; Kim, H. S.; Hwang, S. W.; Roh, J. W.; Yang, D. J.; Shin, W. H.; Li, X. S.; Lee, Y. H.; et al. Dense dislocation arrays embedded in grain boundaries for high-performance bulk thermoelectrics. *Science* **2015**, *348*, 109−114.
(36) Liu, Y.; Zhang, Y.; Ortega, S.; Ibáñez, M.; Lim, K. H.; Grau-Carbonell, A.; Martí-Sánchez, S.; Ng, K. M.; Arbiol, J.; Kovalenko, M. V.; et al. Crystallographically Textured Nanomaterials Produced from the Liquid Phase Sintering of $Bi_xSb_{2-x}Te_3$ Nanocrystal Building Blocks. *Nano Lett.* **2018**, *18*, 2557−2563.
(37) Zhai, R.; Hu, L.; Wu, H.; Xu, Z.; Zhu, T.-J.; Zhao, X.-B. Enhancing thermoelectric performance of n-type hot deformed bismuth-telluride-based solid solutions by nonstoichiometry-mediated intrinsic point defects. *ACS Appl. Mater. Interfaces* **2017**, *9*, 28577−28585.
(38) Hu, L.; Liu, X.; Xie, H.; Shen, J.; Zhu, T.; Zhao, X. Improving thermoelectric properties of n-type bismuth−telluride-based alloys by deformation-induced lattice defects and texture enhancement. *Acta Mater.* **2012**, *60*, 4431−4437.
(39) Seo, S.; Lee, K.; Jeong, Y.; Oh, M.-W.; Yoo, B. Method of efficient Ag doping for Fermi level tuning of thermoelectric Bi0. 5Sb1. 5Te3 alloys using a chemical displacement reaction. *J. Phys. Chem. C* **2015**, *119*, 18038−18045.
(40) Cui, J.; Xue, H.; Xiu, W. Microstructures and thermoelectric properties of p-type pseudo-binary AgxBi0. 5Sb1. 5− xTe3 (x= 0.05−0.4) alloys prepared by cold pressing. *Mater. Lett.* **2006**, *60*, 3669−3672.
(41) Kim, K.; Kim, G.; Lee, H.; Lee, K. H.; Lee, W. Band engineering and tuning thermoelectric transport properties of p-type Bi0. 52Sb1. 48Te3 by Pb doping for low-temperature power generation. *Scr. Mater.* **2018**, *145*, 41−44.
(42) Wei, Z.; Wang, C.; You, L.; Zhao, S.; Yang, K.; Chen, H.; Luo, J.; Chen, X. Significantly enhanced thermoelectric performance of Cu-doped p-type Bi 0.5 Sb 1.5 Te 3 by a hydrothermal synthesis method. *RSC Adv.* **2017**, *7*, 41111−41116.
(43) Huang, Z.; Dai, X.; Yu, Y.; Zhou, C.; Zu, F. Enhanced thermoelectric properties of p-type Bi0. 5Sb1. 5Te3 bulk alloys by electroless plating with Cu and annealing. *Scr. Mater.* **2016**, *118*, 19−23.
(44) Shi, Q.; Zhao, X.; Chen, Y.; Lin, L.; Ren, D.; Liu, B.; Zhou, C.; Ang, R. Cu2Te Incorporation-Induced High Average Thermoelectric Performance in p-Type Bi2Te3 Alloys. *ACS Appl. Mater. Interfaces* **2022**, *14*, 45582−45589.
(45) Chen, B.; Li, J.; Wu, M.; Hu, L.; Liu, F.; Ao, W.; Li, Y.; Xie, H.; Zhang, C. Simultaneous enhancement of the thermoelectric and mechanical performance in one-step sintered n-type Bi2Te3-based alloys via a facile MgB2 doping strategy. *ACS Appl. Mater. Interfaces* **2019**, *11*, 45746−45754.
(46) Li, J.; Tan, Q.; Li, J. F.; Liu, D. W.; Li, F.; Li, Z. Y.; Zou, M.; Wang, K. BiSbTe-based nanocomposites with high ZT: the effect of SiC nanodispersion on thermoelectric properties. *Adv. Funct. Mater.* **2013**, *23*, 4317−4323.
(47) Wu, H.-J.; Yen, W.-T. High thermoelectric performance in Cu-doped Bi2Te3 with carrier-type transition. *Acta Mater.* **2018**, *157*, 33−41.
(48) Chen, J.; Bao, D.; Sun, Q.; Liu, W.-D.; Liu, C.; Tang, J.; Yang, L.; Zhou, D.; Dargusch, M. S.; Chen, Z.-G. Simultaneously optimized thermoelectric performance of n-type Cu2Se alloyed Bi2Te3. *J. Solid State Chem.* **2021**, *296*, 121987.
(49) Yahyaoglu, M.; Ozen, M.; Prots, Y.; El Hamouli, O.; Tshitoyan, V.; Ji, H.; Burkhardt, U.; Lenoir, B.; Snyder, G. J.; Jain, A.; et al. Phase-Transition-Enhanced Thermoelectric Transport in Rickardite Mineral $Cu_{3-x}Te_2$. *Chem. Mater.* **2021**, *33*, 1832−1841.
(50) Akselrud, L.; Grin, Y. WinCSD: software package for crystallographic calculations (Version 4). *J. Appl. Crystallogr.* **2014**, *47*, 803−805.
(51) Snyder, G. J.; Snyder, A. H. Figure of merit ZT of a thermoelectric device defined from materials properties. *Energy Environ. Sci.* **2017**, *10*, 2280−2283.
(52) Lee, C.-h.; Dharmaiah, P.; Kim, D. H.; Yoon, D. K.; Kim, T. H.; Song, S. H.; Hong, S.-J. Synergistic Optimization of the Thermoelectric and Mechanical Properties of Large-Size Homogeneous Bi0. 5Sb1. 5Te3 Bulk Samples via Carrier Engineering for Efficient Energy Harvesting. *ACS Appl. Mater. Interfaces* **2022**, *14*, 10394−10406.
(53) Yu, H. J.; Jeong, M.; Lim, Y. S.; Seo, W.-S.; Kwon, O.-J.; Park, C.-H.; Hwang, H.-J. Effects of Cu addition on band gap energy, density of state effective mass and charge transport properties in Bi 2 Te 3 composites. *RSC Adv.* **2014**, *4*, 43811−43814.
(54) Han, M.-K.; Ahn, K.; Kim, H.; Rhyee, J.-S.; Kim, S.-J. Formation of Cu nanoparticles in layered Bi 2 Te 3 and their effect on ZT enhancement. *J. Mater. Chem.* **2011**, *21*, 11365−11370.
(55) Shannon, R. D. Revised effective ionic radii and systematic studies of interatomic distances in halides and chalcogenides. *Acta Crystallogr. Sect. A Cryst. Phys. Diffr. Theor. Gen. Crystallogr.* **1976**, *32*, 751−767.
(56) Sepehri-Amin, H.; Imasato, K.; Wood, M.; Kuo, J. J.; Snyder, G. J. Evolution of Nanometer-Scale Microstructure within Grains and in the Intergranular Region in Thermoelectric Mg3 (Sb, Bi) 2 Alloys. *ACS Appl. Mater. Interfaces* **2022**, *14*, 37958−37966.
(57) Femi, O. E.; Elangovan, H.; Mukherjee, S.; Tripathi, S.; Chattopadhyay, K. Thermoelectric properties of BiSbTe-type alloys prepared by chill-casting and cryo-milling. *Mater. Chem. Phys.* **2021**, *260*, 124116.
(58) Kim, H.-S.; Gibbs, Z. M.; Tang, Y.; Wang, H.; Snyder, G. J. Characterization of Lorenz number with Seebeck coefficient measurement. *Apl. Mater.* **2015**, *3*, 041506.
(59) Ahmad, K.; Wan, C.; Zong, P.-a. Thermoelectric properties of BiSbTe/graphene nanocomposites. *J. Mater. Sci.: Mater. Electron.* **2019**, *30*, 11923−11930.
(60) Kim, I.-H.; Choi, S.-M.; Seo, W.-S.; Cheong, D.-I. Thermoelectric properties of Cu-dispersed bi 0.5 sb 1.5 te 3. *Nanoscale Res. Lett.* **2012**, *7*, 2−6.
(61) Pan, Y.; Wei, T.-R.; Wu, C.-F.; Li, J.-F. Electrical and thermal transport properties of spark plasma sintered n-type Bi 2 Te 3− x Se x alloys: The combined effect of point defect and Se content. *J. Mater. Chem. C* **2015**, *3*, 10583−10589.
(62) Yang, G.; Sang, L.; Yun, F. F.; Mitchell, D. R.; Casillas, G.; Ye, N.; See, K.; Pei, J.; Wang, X.; Li, J. F.; et al. Significant Enhancement of Thermoelectric Figure of Merit in BiSbTe-Based Composites by Incorporating Carbon Microfiber. *Adv. Funct. Mater.* **2021**, *31*, 2008851.
(63) Yang, G.; Niu, R.; Sang, L.; Liao, X.; Mitchell, D. R.; Ye, N.; Pei, J.; Li, J. F.; Wang, X. Ultra-High Thermoelectric Performance in Bulk BiSbTe/Amorphous Boron Composites with Nano-Defect Architectures. *Adv. Energy Mater.* **2020**, *10*, 2000757.
(64) Yang, S. E.; Kim, F.; Ejaz, F.; Lee, G. S.; Ju, H.; Choo, S.; Lee, J.; Kim, G.; Jung, S.-h.; Ahn, S.; et al. Composition-segmented BiSbTe thermoelectric generator fabricated by multimaterial 3D printing. *Nano Energy* **2021**, *81*, 105638.
(65) Shi, F.; Wang, H.; Zhang, Q.; Tan, X.; Yin, Y.; Hu, H.; Li, Z.; Noudem, J. G.; Liu, G.; Jiang, J. Improved Thermoelectric Properties of BiSbTe-AgBiSe2 Alloys by Suppressing Bipolar Excitation. *ACS Appl. Energy Mater.* **2021**, *4*, 2944−2950.
(66) Madavali, B.; Lee, C. H.; Kim, H. S.; Lee, K. H.; Hong, S. J. Investigation of microstructure and thermoelectric properties of p-type BiSbTe/ZnO composites. *Int. J. Appl. Ceram. Technol.* **2018**, *15*, 125−131.

https://doi.org/10.1021/acs.chemmater.3c00229
Chem. Mater. 2023, 35, 3603−3613

(67) Madavali, B.; Kim, H.-S.; Lee, K.-H.; Hong, S.-J. Enhanced Seebeck coefficient by energy filtering in Bi-Sb-Te based composites with dispersed Y2O3 nanoparticles. *Intermetallics* **2017**, *82*, 68−75.
(68) Madavali, B.; Sharief, P.; Park, K.-T.; Song, G.; Back, S.-Y.; Rhyee, J.-S.; Hong, S.-J. Development of high-performance thermoelectric materials by microstructure control of p-type BiSbTe based alloys fabricated by water atomization. *Materials* **2021**, *14*, 4870.
(69) Madavali, B.; Kim, H.; Hong, S.-J. Reduction of thermal conductivity in Al2O3 dispersed p-type bismuth antimony telluride composites. *Mater. Chem. Phys.* **2019**, *233*, 9−15.
(70) Sie, F.-R.; Hwang, C.-S.; Kuo, C.-H.; Chou, Y.-W.; Yeh, C.-H. Enhanced thermoelectric properties of P-type BiSbTe/TiO2Ag alloys. *Intermetallics* **2019**, *109*, 30−36.
(71) Zheng, Y.; Zhang, Q.; Su, X.; Xie, H.; Shu, S.; Chen, T.; Tan, G.; Yan, Y.; Tang, X.; Uher, C.; et al. Mechanically robust BiSbTe alloys with superior thermoelectric performance: a case study of stable hierarchical nanostructured thermoelectric materials. *Adv. Energy Mater.* **2015**, *5*, 1401391.

Recommended by ACS

Enhanced Thermoelectric Properties of $Zr_{0.85-x}Hf_xNb_{0.15-y}Ta_yCoSb$ Medium-Entropy Alloys: Tradeoff between "What to Alloy" and "How Much to Al...

Rongchun Chen, Tongmin Wang, *et al.*
FEBRUARY 28, 2023
CHEMISTRY OF MATERIALS
READ

Reversible Thermal Conductivity Modulation of Non-equilibrium $(Sn_{1-x}Pb_x)S$ by 2D–3D Structural Phase Transition above Room Temperature

Zhongxu Hu, Toshio Kamiya, *et al.*
MARCH 04, 2023
ACS APPLIED ENERGY MATERIALS
READ

Investigation of Dielectric, Ferroelectric, and Strain Responses of $(1 - x)[0.90(Bi_{0.5}Na_{0.5})TiO_3 - 0.10SrTiO_3] - xCuO$ Ceramics

Amir Ullah, Abid Zaman, *et al.*
MARCH 21, 2023
ACS OMEGA
READ

Endotaxial Intergrowth of Copper Telluride in GeTe-Rich Germanium Antimony Tellurides Leads to High Thermoelectric Performance

Stefan Schwarzmüller, Oliver Oeckler, *et al.*
NOVEMBER 03, 2022
CHEMISTRY OF MATERIALS
READ

Get More Suggestions >

https://doi.org/10.1021/acs.chemmater.3c00229
Chem. Mater. 2023, 35, 3603−3613